Research Square

Preprints are preliminary reports that have not undergone peer review.
They should not be considered conclusive, used to inform clinical practice,
or referenced by the media as validated information.

Chromatin Binding Enriches RNA Polymerase II in Transcription Condensates

Jan-Hendrik Spille

jhspille@uic.edu

University of Illinois Chicago https://orcid.org/0000-0001-8493-4721

Alisha Budhathoki

University of Illinois Chicago

Ganesh Pandey

University of Illinois Chicago

Filmon Medhanie

University of Illinois Chicago

Gia-Han Ngo

University of Illinois Chicago

Salmana Mahmood

University of Illinois Chicago

Article

Keywords:

Posted Date: August 14th, 2025

DOI: https://doi.org/10.21203/rs.3.rs-7302634/v1

License: This work is licensed under a Creative Commons Attribution 4.0 International License.
Read Full License

Additional Declarations: There is **NO** Competing Interest.

Chromatin Binding Enriches RNA Polymerase II in Transcription Condensates

Author Information

Affiliations

Department of Physics, University of Illinois Chicago, Chicago, IL, USA

Alisha Budhathoki, Ganesh Pandey, Filmon Medhanie, Gia-Han Ngo, Salmana Mahmood & Jan-Hendrik Spille

Current address: Molecular Surgery Laboratory, Department of Ophthalmology, Byers Eye Institute, Stanford University, Palo Alto, CA, USA

Gia-Han Ngo

Contributions

Conceptualization: A.B., G.P., F.M., and J.H.S. Methodology: A.B., G.P., F.M., and J.H.S. Investigation: A.B., G.P., F.M., G.H.N., S.M., and J.H.S. Formal analysis: A.B., G.P., F.M. Software: A.B., G.P. Visualization: A.B., G.P., and F.M. Funding acquisition: J.H.S. Project administration: J.H.S. Supervision: A.B., F.M., and J.H.S. Writing – original draft: A.B., F.M., and J.H.S. Writing – review & editing: A.B., G.P., F.M., and J.H.S.

Corresponding author

Correspondence to: Jan-Hendrik Spille (jhspille@uic.edu)

Abstract

The small size of transcription condensates prevents characterization of their material properties with conventional assays. Here, we use single particle tracking to observe individual RNA Polymerase II molecules inside transcription condensates in mouse embryonic stem cells. We find that Pol II inside transcription condensates is overwhelmingly in an immobile state. Super-resolution microscopy of the Serine 5-phosphorylated isoform identifies this fraction as chromatin-bound. In contrast to *in vitro* experiments, the Pol II C-terminal domain partitions into condensates only weakly in live cells. Notably, Pol II is dispensable for condensate maintenance. The Mediator fraction persists when Pol II is purged from condensates. Our results suggest that mobile Pol II can readily shuttle across the boundary of Mediator condensates as a passive client and is enriched in the condensate phase through chromatin binding and transcription initiation. Understanding molecular interactions within condensates is crucial for the development of biophysical models of condensate function.

Introduction

A phase separation model has been proposed to explain how mammalian cells can efficiently gather the dozens of factors involved in transcription regulation at a target gene [1]. Experimental evidence shows that transcription condensates concentrate key components of the transcription machinery at super-enhancer gene loci [1–5]. Prominent condensate constituents include the coactivator Brd4 [1], the Mediator complex [1,2], and RNA Polymerase II (Pol II) [2]. Transcription factors may contribute to condensate formation [4,6] and recruitment of Pol II to condensates [7]. Local RNA concentration has been proposed as a regulator of condensate lifetime and growth through reentrant phase separation [8].

Transcription condensates fuse upon contact, rapidly exchange constituent molecules with the surrounding nucleoplasm, and are sensitive to 1,6-hexanediol [1,2]. These properties are consistent with liquid-like material properties, thought to be facilitated by weak, multivalent interactions between

intrinsically disordered protein regions (IDRs) that are abundant in components of the transcription machinery [1]. Examples include transcription factor activation domains [4,9], the C-terminal domain of Brd4 that has also been used to induce synthetic condensates [10], and the low complexity Pol II C-terminal domain (CTD) consisting of $Y_1S_2P_3T_4S_5P_6S_7$ heptapeptides (52 heptad repeats in mouse and human cells) [11]. Changing the CTD length modulates Pol II transient clustering dynamics in live cell nuclei [12].

In vitro, the IDRs of known transcription condensate constituents coalesce through liquid-liquid phase separation [1,12,13], e.g. the Brd4-IDR and the Pol II CTD partition into Med1-IDR droplets [4,14,15]. Fusing a suitable IDR to a protein of interest is sufficient to enrich this protein in such droplets [16,17]. Together, these findings gave rise to the prevalent model of transcription condensates in which interactions between their IDRs cause Brd4, Mediator, and Pol II to locally enrich in dense phase foci through a phase separation process mediated. In this model, condensates are seeded by locally enriched binding of transcription factors and Brd4 [18] to chromatin as well as low amounts of RNA [8].

But *in vitro* reconstitutions are necessarily of reduced complexity and may not fully mirror the behavior of endogenous proteins in living cells. *In vivo*, the small size of transcription condensates at or below the diffraction-limited resolution of optical microscopy complicates quantitative interpretation of experimental data. In particular, fluorescence recovery after photobleaching (FRAP) experiments yield exchange kinetics of condensate constituents [1,2] but cannot resolve dynamics of internal rearrangement [19,20]. Hence, FRAP is not suited to determine quantitative parameters of a kinetic condensate model.

We reasoned that single particle tracking with bright fluorophores would provide sufficient spatial localization precision to overcome this limitation [21]. Under realistic conditions, single fluorescently labeled proteins can be localized with $\leq 20\ nm$ precision, while transcription condensates have a diameter of up to $500\ nm$. Previous studies have used single particle tracking to investigate the condensate nature of bacterial RNA polymerase clusters [22] and to assert that Pol II accumulates in viral replication compartments through nonspecific protein-DNA interactions [23] rather than a phase separation

process. Single particle tracking further yielded insight into transcription factor dynamics in nuclear condensates [24,25].

Here, we used CRISPR/Cas9 genome editing to fuse a SNAP-tag [26] to the endogenous Rpb1 subunit of RNA Pol II in mouse embryonic stem cells (v6.5) as previously described [2]. We then labelled SNAP-Pol II with photo-activatable JF646 SNAP-ligand [27] and obtained single Pol II tracking data at 10ms temporal resolution. Concomitant labelling of SNAP-Pol II with JF554X SNAP-ligand [28] allowed us to identify transcription condensate positions in reference images and relate Pol II trajectories to endogenous condensates. To our surprise, Pol II inside condensates exhibited very low mobility compared to the surrounding nucleoplasm, consistent with a chromatin-bound state. A more detailed single trajectory mobility analysis revealed that freely diffusive Pol II can access the condensate volume but is not enriched there over the surrounding nucleoplasm. Only molecules in the bound state contribute to Pol II enrichment in transcription condensates. Two-color super-resolution microscopy of general Pol II and its Serine-5 phosphorylated (initiating/transcribing) isoform corroborates this finding. Most of the transcription condensate volume is filled with phosphorylated, and therefore chromatin-bound Pol II.

The prevailing model of transcription condensates postulates that homo- and heterotypic, weak, multivalent interaction between the Pol II CTD and IDRs in the condensate phase are responsible for Pol II partitioning into condensates [5,29]. To investigate the contribution of such interactions to Pol II enrichment in condensates, we expressed a Pol II CTD fused to the HaloTag [30] in our cellular system. We found that Halo-CTD was only weakly enriched in condensates in both widefield image analysis and at single molecule resolution. In some cells, Halo-CTD formed diffraction-limited clusters, but these did not overlap with Pol II foci. This observation demonstrates that in contrast to the prevailing model, the Pol II CTD does not play a major role in transcription condensate formation. The fact that Pol II and its CTD are dispensable for condensate integrity is underscored by the fact that the Mediator fraction in condensates remains virtually unchanged under acute Pol II degradation.

Collectively, our findings clearly demonstrate that the current paradigm of Pol II recruitment to *in vivo* transcription condensates through weak and transient interactions of its CTD is incomplete. We propose that Pol II is enriched in transcription condensates because it can very efficiently get loaded onto DNA and intiate transcription inside the condensate phase, rather than because of phase separation mediated by its intrinsically disordered C-terminal domain. A more accurate model of transcription condensates should treat Pol II as a passive client to an existing condensate phase, likely formed by Brd4 and Mediator at highly acetylated chromatin regulatory elements.

Results

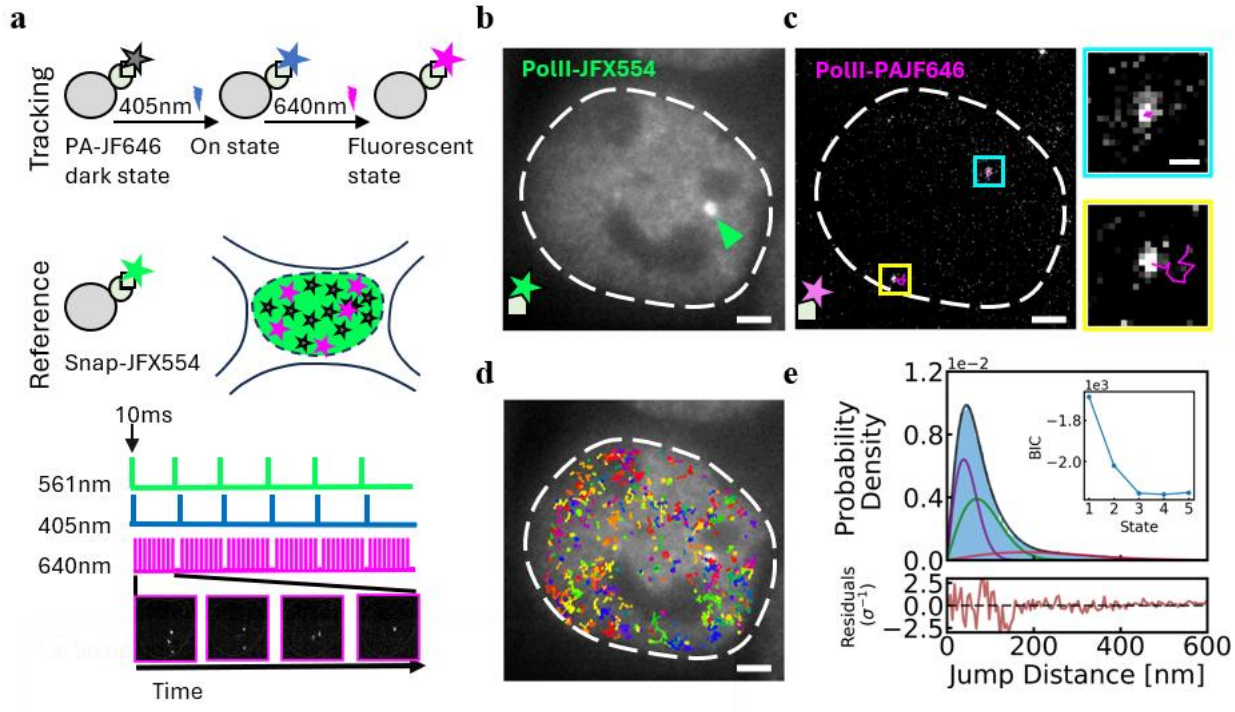
Global mobility of RNA Pol II in mouse embryonic stem cells.

We first sought to determine the mobility of RNA Pol II in v6.5 mouse embryonic stem cells (mESCs) globally. We used CRISPR/Cas9 technology to attach a SNAP-tag polypeptide to the N-terminus of Rpb1, the largest subunit of RNA Pol II as previously described [2]. Both alleles were edited, and scarless insertion was verified using sequencing (**Suppl. Fig. 1**). We then used live cell-permeable fluorescent SNAP-ligands in a dual-color labeling scheme (**Fig. 1a**) to track the dynamics of endogenous Pol II molecules. Low concentrations of SNAP-JFX554 [28] or SNAP-TMR ligand highlighted the global Pol II distribution in reference images. This allowed us to segment mESC nuclei and identify transcription condensate positions (**Fig. 1b**). Simultaneously, we used photoactivatable SNAP-PAJF646 for single particle tracking at 10ms temporal resolution in the same cells (**Fig. 1c, Suppl. Vid. 1**). To minimize linkage errors during tracking [31], we obtained sparse data in multiple acquisition cycles from each nucleus. On average, we detected at most 1.5 particles per nucleus in each image frame (**Suppl. Fig. 2**). Each acquisition cycle consisted of a reference image taken with 561nm excitation of SNAP-JFX554

or SNAP-TMR (1 frame) followed by photo-activation of SNAP-PAJF646 (405nm, 1 frame), and subsequent tracking of the photo-activated molecules (640nm, 498 frames) (**Fig. 1a**). Each acquisition cycle lasted approximately 5 seconds. This experimental protocol yielded several hundred trajectories per nucleus in 10-15 cycles per nucleus (**Fig. 1d**). Pol II single molecule signals were localized with subpixel precision using ThunderSTORM [32] and connected to trajectories using custom Python scripts using a Hungarian algorithm with a maximum allowed displacement of 600nm.

As expected, we observed both bound and diffusive Pol II molecules (**Fig. 1c**, insets). The jump distance probability distribution was best described by a three state model (accounting for experimentally determined localization precision [31,33]) according to the Bayesian Information Criterion (BIC)[34] (**Fig. 1e**; **Suppl. Fig. 3**): A mobile fraction with diffusion coefficient $D_3 = 1.57 \pm 0.11\ \mu m^2/s\ (s.d.)$ accounting for a fraction of $15.1\ \% \pm 0.5\ \%\ (\mathrm{s.d.})$ that we interpret to represent unbound, diffusive Pol II. A low mobility fraction ($D_1 = 0.03 \pm 0.01\ \mu m^2/s$, $40.8\ \% \pm 0.6\ \%$) most likely representing DNA-bound Pol II, and an intermediate fraction with low diffusion coefficient $D_2 = 0.19 \pm 0.03\ \mu m^2/s$ accounting for $44.1\ \% \pm 0.9\ \%$ of jumps. Using a more sophisticated analysis accounting for measurement artifacts (Spot-on)[35] yielded comparable results (**Suppl. Fig. 4**). Our observations are consistent with previous reports of Pol II mobility in U2OS [12,36] and budding yeast cells [37].

Fig. 1: Pol II single particle tracking in mESC.



a Two-color labeling scheme for endogenous Snap-Pol II and image acquisition protocol. Each nucleus was subjected to 10-15 imaging cycles of 1 reference frame (561nm excitation), 1 activation frame (405nm), and 498 tracking frames (640nm) at 10ms exposure time. **b** Reference images were used to segment nuclei (dashed white line) and identify condensate regions (green arrowhead). **c** Pol II single molecule tracks were obtained by sparse activation of PAJF646-labeled Snap-Pol II. Insets: Examples of a bound (cyan frame, top) and a mobile (yellow frame, bottom) Pol II track. **d** This approach yielded several hundred tracks per nucleus for a total of 128,563 from 269 cells. **e** Jump distance analysis of a sample 25000 jumps randomly chosen out of 476918 total. The probability distribution was best described by a three-state model including a bound state (purple), a low mobility state (green), and a fast diffusive state (red). Bottom panel: Fit residuals. Inset: Bayesian Information Criterion values for 1-5 state models. Scale bars: **b**, **c**, **d** 2 µm. Insets 200nm.

Mobility of Pol II inside transcription condensates

Next, we sought to determine how transcription condensates modulate the mobility of Pol II with respect to these global values. Condensates are readily identified as diffraction-limited bright foci in the reference images acquired during each acquisition cycle (**Fig. 1d**). Since Pol II is enriched in these condensates over the surrounding nucleoplasm, we expected to find a higher trajectory density in them. But limiting the analysis to tracks at condensates also reduces the region of interest by orders of magnitude. Hence, in any given nucleus only a few out of hundreds of trajectories traversed the condensate volume (**Fig. 2a, Suppl. Vid. 2**). To collect sufficient data for the statistical analysis of single molecule dynamics, we aligned Pol II trajectories from all cells and acquisition cycles with respect to condensate coordinates. To this end, we used Gaussian peak fitting with a precision of tens of nanometers to determined the centroid coordinates of each diffraction-sized condensate (**Fig. 2a**, top and bottom). We then subtracted the coordinates of the nearest condensate from each trajectory and overlaid the resulting tracks (**Fig. 2b, Suppl. Vid. 3**).

The radial distribution of single molecule localization density with respect to condensate centroids and the widefield resolution image intensity both peak at the condensate centroid and have a radial spread of approximately 250nm (**Fig. 2b,c**). This matches condensate sizes determined from fixed cell super-resolution microscopy (**Fig. 4, Suppl. Fig. 5**).

But despite the higher precision afforded by single molecule localization microscopy, it is not possible to define clear boundaries for individual condensates. Single molecule tracking localizations from single molecules are too sparse. Likewise, it is not possible to obtain accurate condensate outlines from diffraction-limited widefield images due to the small condensate size (**Fig. 2b**, top). Color-coding each track by it mobility makes it evident that tracks inside the condensate volume predominantly represent the lowest mobility states (blue), whereas mobile tracks (yellow) are almost entirely excluded from the condensate volume (**Fig. 2d**). Hence, we reasoned that we would be able to use this observation to determine a radial threshold, below which displacements should be considered inside the condensate. We

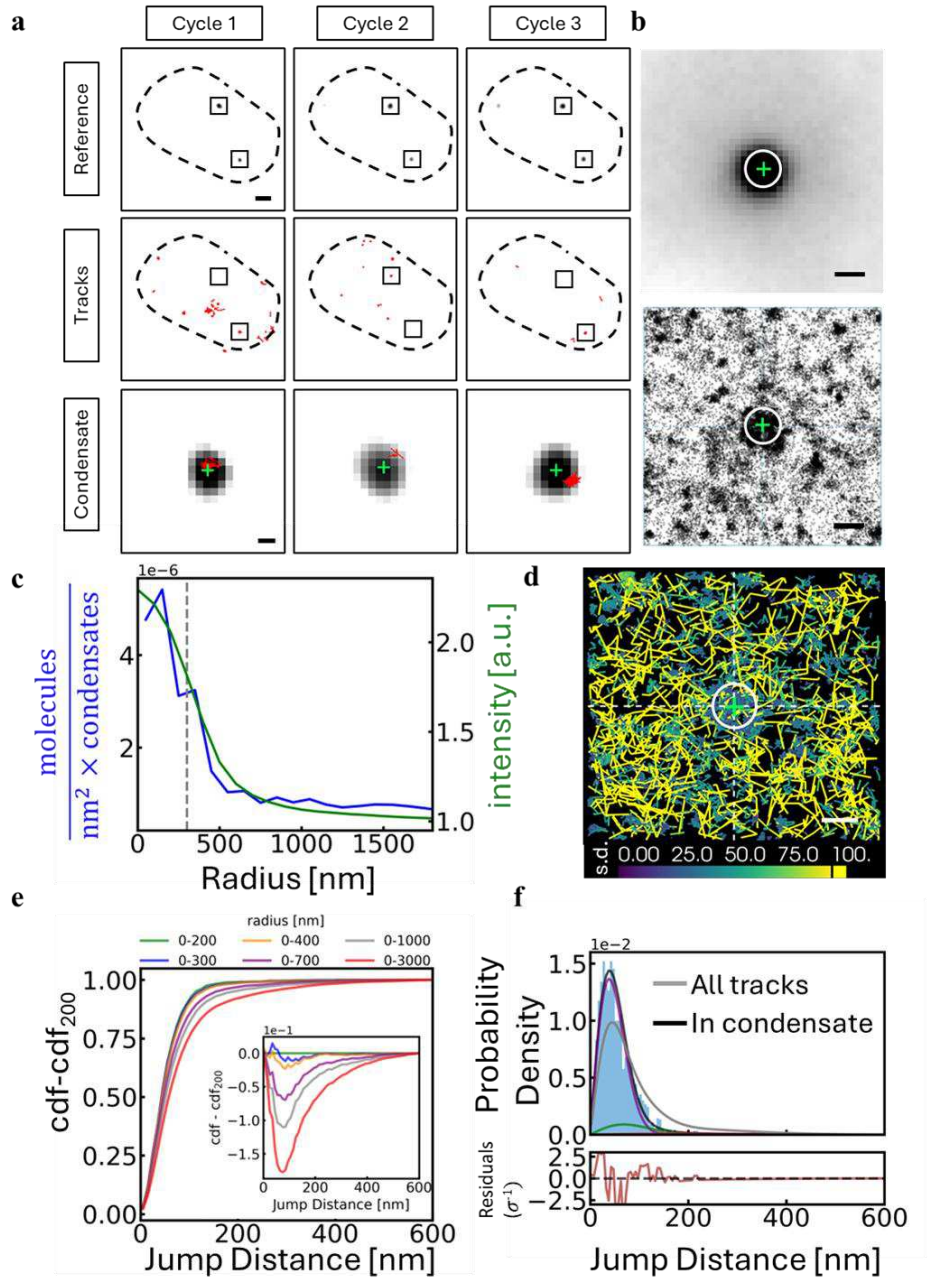
calculated the cumulative density function (CDF) of Pol II displacements within varying radial cutoffs down to 200nm from the condensate centroid (**Fig. 2e**). Generally, reducing the threshold radius shifted the CDF towards shorter displacements, i.e. lower mobility. Below 400nm, the CDF approached a stable shape and differences between 200nm and 300nm radial thresholds were negligible. Therefor we consider all localizations located less than 300nm from the condensate centroid to be confidently "inside" the condensate volume for further analysis.

By this metric, a total of 565 Pol II trajectories had at least one localization detected inside a condensate. To avoid misclassifications, we only considered tracks for which the respective condensate was observed during the same acquisition cycle. The CDF analysis (**Fig. 2e**) already indicated that Pol II inside condensates is less mobile. Accordingly, the jump distance distribution of Pol II tracks fully contained inside condensates is shifted to smaller values (**Fig. 2f**) compared to global results (**Fig. 1**). We employed a global fitting strategy to facilitate the comparison of jump distance data between different conditions by focusing on changes in relative fractions while holding diffusion coefficients constant (**Methods**). We find that in condensates, the most mobile Pol II population is highly diminished ($15.1\ \% \pm 0.5\ \%$ globally $\rightarrow 3.2\ \% \pm 0.9\ \%$ inside condensates), and so is the intermediate mobility population ($44.1\ \% \pm 0.9\ \%$ globally $\rightarrow 8.8\ \% \pm 3.2\ \%$ inside). In contrast, the bound state is highly abundant inside condensates ($40.8\ \% \pm 0.6\ \%$ globally $\rightarrow 88.0\ \% \pm 2.7\ \%$ inside).

Limiting the analysis to tracks fully contained within condensates may bias the outcome towards low mobility particles. To rule out such artifacts, we repeated the analysis for all displacements inside condensates from any track, and included displacements that have only one localization inside the radial threshold, i.e. those that cross the condensate boundary. These less stringent criteria shift the mobility distribution inside condensates only slightly towards higher mobility (**Suppl. Fig. 6**).

The analysis so far indicates a highly reduced mobility of Pol II inside condensates. This may result from either a high effective viscosity or confinement of Pol II inside the condensate phase. But the jump distance distribution model (**Fig. 1e, 2f**) represents a linear combination of freely diffusive states. Hence, this analysis cannot inform on more complex behavior such as anomalous diffusion or confinement.

Fig. 2: Pol II in condensates is mostly in the bound state.



a In each imaging cycle, condensate ROIs are identified from reference images (top). Pol II tracks (middle, red) are aligned with respect to condensate centroids (green cross, bottom). **b** Sum of condensate reference ROIs at widefield resolution (top), and Pol II single molecule localizations (middle) from all cycles aligned by centroid coordinates. **c** Radial density of the accumulated reference image intensity

(green) and single molecule localizations density (blue) indicate the condensate size. **d** Pol II trajectories colored by mobility. White circles represent a 300nm radius used for condensate segmentation. **e** CDFs converge to the reference distribution (200nm radial cutoff) at below 400nm radial threshold. **f** Jump distance analysis yields a high bound fraction for tracks inside condensates (scale bars: **a** (top) 2µm, **a** (bottom) 200nm, **b**, **d** 500nm.

Bound, but not mobile Pol II partitions into condensates

We reasoned that a single trajectory mean-squared displacement (MSD) analysis would allow us to further scrutinize the nature of Pol II tracks and uncover confinement in condensates or subdiffusive behavior. Fitting the particle MSD with the anomalous diffusion equation $MSD(\Delta t) = 4D^*\Delta t^\alpha$ yields an exponent α and a generalized diffusion coefficient D^* for each Pol II track. Isotropic Brownian diffusion results in $\alpha = 1$, whereas confined or sub-diffusive motion is characterized by $\alpha < 1$.

We calculated the MSD for all 28267 trajectories with a minimum length of 5 jumps (60ms) and plotted the results in a 2D histogram of the exponent α and $\log(D^*)$ (**Fig. 3a**). This histogram was best described by a three-state Gaussian mixture model as judged by the BIC. Each component of the Gaussian mixture model is characterized by a mean exponent $\langle\alpha_i\rangle$ and mean generalized diffusion coefficient $\langle D_i^*\rangle$. We find a high mobility state accounting for 19% of the tracks with generalized diffusion coefficient $\langle D_3^*\rangle = 0.78\ \mu m^2/s^\alpha$ that represents "freely diffusive" Pol II as judged by its mean exponent ($\langle\alpha_3\rangle = 0.945 \pm 0.006\ (s.e.m)$). This population of tracks appears clearly distinct in the 2D histogram. Two low-mobility states partially overlap in the 2D histogram. They are best characterized as "fully bound" (57% of tracks with $\langle D_1^*\rangle = 0.0024\ \mu m^2/s^\alpha$) and $\langle\alpha_1\rangle = 0.177 \pm 0.003\ (s.e.m)$) and "low mobility sub-diffusive" (24% of tracks, $\langle D_2^*\rangle = 0.023\ \mu m^2/s^\alpha, \langle\alpha_2\rangle = 0.592 \pm 0.005\ (s.e.m)$). The population MSDs for each component were well fit by a power law $MSD(\Delta t) = 4D^*\Delta t^\alpha$ which yields similar results for D^* and α for each of the components (**Supp. Fig. 7**).

This qualitative characterization of the states is reflected in the angular probability distributions [38] of consecutive jumps (**Fig. 3b**). The highest mobility state (component 3) exhibits an isotropic angular distribution as expected for freely diffusing particles. In contrast, the two lower mobility states have highly anisotropic angular jump distributions indicative of sub-diffusive or bound particles. As a control, we tracked H2B-Halo transiently transfected into mESCs. Performing the same single track MSD analysis on the data yielded a two-state model as previously reported [39,40] with mobility states and their relative proportion matching the two Pol II states of lower mobility (**Suppl. Fig. 8**). These results suggest that both low mobility states represent Pol II engaged with chromatin [41].

The single-track MSD analysis allowed us to assign each Pol II trajectory to one of the three mobility states and to analyze their spatial distribution throughout the cell nucleus (**Suppl. Fig. 9**). Generally, all three states are distributed throughout the cell nucleus. When we again align all tracks with respect to the nearest condensate centroid, a more nuanced picture emerges. Pol II of all three mobility states ranging from bound to freely diffusive is present in the condensate volume (**Fig. 3d**). This observation in itself is at odds with a model that describes the condensate phase as "liquid-like" but with different viscosity. Notably, it is predominantly the least mobile, bound population that contributes to Pol II enrichment inside condensates. This is immediately evident when we plot the normalized radial distribution of track density for the different populations (**Fig. 3c**). To account for the fact that faster moving particles result in shorter trajectories with fewer localizations, we considered only the mean coordinate of each track for this analysis. We then calculated partition coefficients for molecules assigned to each of the three mobility states by dividing the average density inside condensates ($r<300nm$) by the density in a reference region far from the condensate ($700nm < r < 1500nm$). The relative partition coefficients for freely diffusive molecules (1.7x) and low mobility sub-diffusive molecules (2.7x) are small compared to the value for molecules in the least mobile, bound state (15.7x) (**Fig. 3c** inset). We note that this last component also accounts for the largest fraction of tracks, highlighting even further that Pol II enrichment inside condensates results predominantly from the bound, and not the mobile molecules (**Suppl. Fig. 9**).

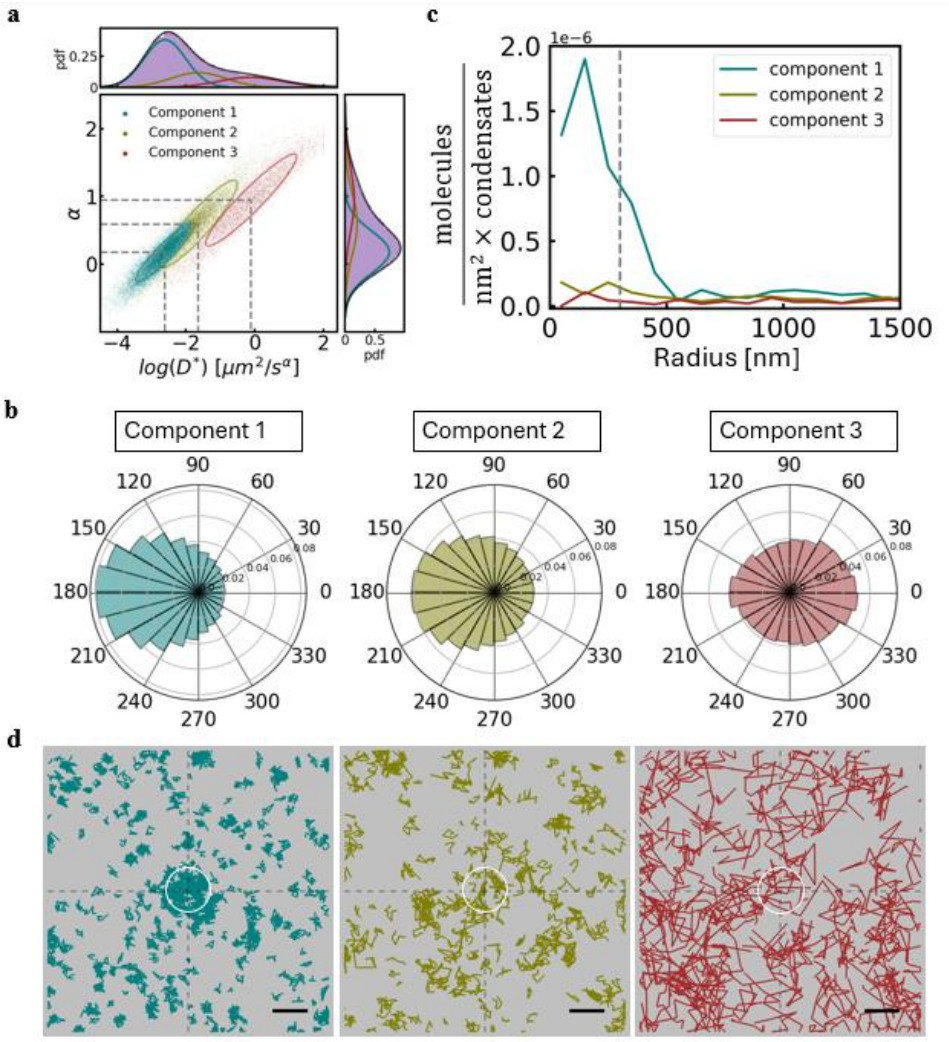
This surprising finding is corroborated by an analysis of boundary crossing trajectories (**Suppl. Fig. 10**). To confidently ascertain that tracks crossed our radial condensate threshold, we required them to be localized inside and outside a buffer zone with width of twice the localization precision, i.e. cross an annular zone ranging from 280nm to 320nm from the condensate centroid. Only a small number of trajectories fulfilled these strict criteria and clearly crossed the condensate boundary. We found that separating boundary crossing tracks based on the direction of crossing revealed asymmetric behavior (**Suppl. Fig. 10a**). Tracks originating outside the condensate *i)* displayed more long displacements (>200nm), *ii)* diffused far into the condensate volume, and *iii)* retained higher mobility inside the condensate. In contrast, trajectories that originated inside the condensate and crossed to the exterior *i)* were of much lower mobility with few long displacements, *ii)* originated from the edge of the condensate, and *iii)* had low mobility matching the bound state while still inside the condensate as evident from a comparison of CDFs for the different conditions (**Suppl. Fig. 10b**).

Based on a set of observations, we propose a model for Pol II interaction with the condensate phase: Particles first observed outside condensates are slightly less mobile inside condensates than the freely diffusive population but retain a higher mobility than those first observed inside condensates. Hence, mobile Pol II can readily enter the condensate volume from the outside and explore the condensate volume. Most tracks entering the condensate are not observed to leave it again (**Suppl. Fig. 10**). Therefore, Pol II gets captured efficiently inside condensates, likely through DNA binding. We do not observe Pol II to hop between binding sites inside condensates. Once captured, Pol II stays bound to chromatin rather than exploring the condensate interior. Tracks exiting the condensate originate from the edge of the condensate and show long displacements only outside the condensate. We speculate that this may reflect transcription termination events.

These results are remarkable because transcription condensates are commonly described as being in a "liquid-like" state, in which condensate constituent molecules are only loosely associated with each other and able to readily rearrange within the condensate phase [1,2,4]. We do not observe such behavior for Pol II

at the single molecule level. Instead, our data shows that mobile Pol II can diffuse through the condensate volume with only minor changes in mobility while bound the vast majority of Pol II inside condensates is in a tightly bound state. We hypothesized that this state reflects Pol II bound to DNA, possibly engaged in transcription.

Fig. 3: Single trajectory analysis



a α vs $\log_{10}(D^*)$ histogram from single trajectory MSD analysis. The probability distribution functions of both parameters are best described by a three-component model. Colored ovals indicate centers and

spreads of the three components in a Gaussian mixture model best describing the full dataset. **b** Angular distribution plots show that component 1 (teal) mobility is highly anisotropic, i.e. tightly bound, with a fold-anisotropy metric $f_{180/0} = 3.45$. Component 2 (yellow) is sub-diffusive ($f_{180/0} = 2.04$), while component 3 is freely diffusive ($f_{180/0} = 0.89$). **c** Radial distribution of normalized track density for each of the components. Component 2 (2.3x) and 3 (4.2x) are mildly enriched in condensates, while the bound component 1 is highly enriched (19.0x). **d** Aligning trajectories from each component relative to the condensate centroid shows that mobile Pol II can traverse the condensate volume while bound tracks are highly enriched. Scale bar: 500nm.

Pol II in condensates is bound to chromatin

To test the hypothesis that immobile Pol II in condensates is bound to chromatin, we sought to determine its functional state using phospho-specific immuno-staining and fixed cell super-resolution microscopy. Previously, we had demonstrated that transcription condensates are sites of productive elongation using nascent RNA labeling [2]. We reasoned that the fraction of Pol II engaged in productive elongation should be reflected in detectable levels of Pol II phosphorylation.

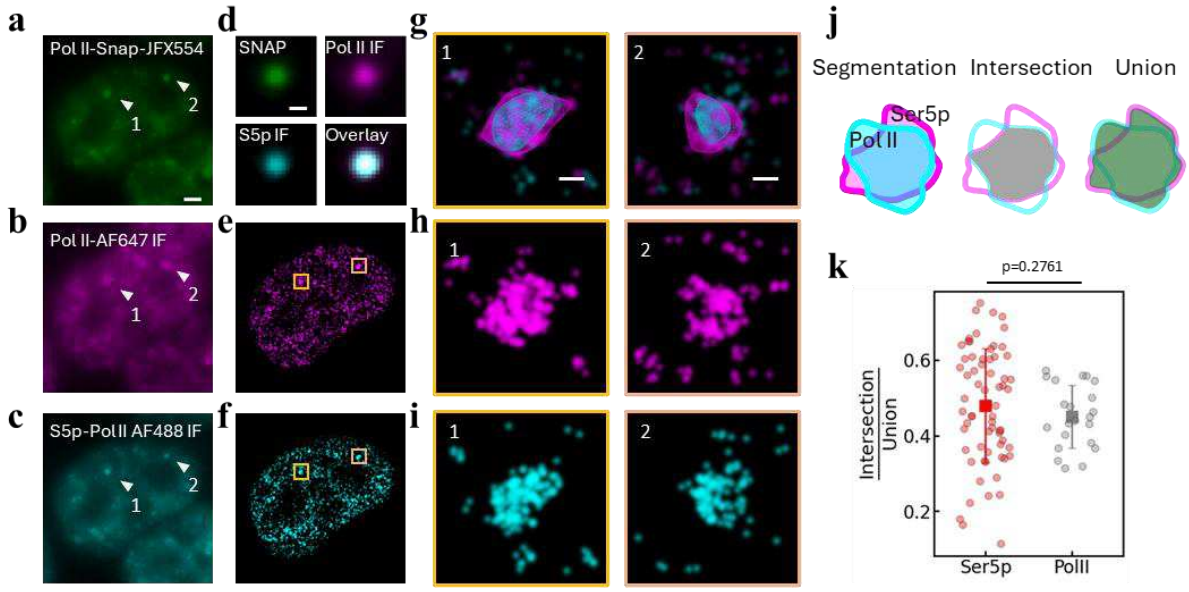
To assess the degree of Pol II phosphorylation in condensates, we labeled endogenous Pol II in our CRISPR-edited cell line simultaneously in three different ways: *i)* with Snap-JFX554 as described above to obtain reference images of global Pol II organization (**Fig. 4a**, see also **Fig. 1b, 2a**); *ii)* by immunofluorescence with an antibody directed against all isoforms of Pol II (**Fig. 4b**); and *iii)* by orthogonal immunofluorescence with an antibody specific to the Serine 5-phosphorylated (S5p) isoform of Pol II that is found during transcription initiation and early productive elongation (**Fig. 4c**). We then acquired conventional resolution reference images of all three channels as described for the single particle tracking experiments, followed by two-color 3D direct stochastic optical reconstruction microscopy (dSTORM) images [42] of general Pol II and S5p-specific immunostaining signal.

311 Indeed, we were able to visually identify condensates in all three detection channels (**Fig. 4a-c**). Notably,
312 all individual condensates identified in the Snap-Pol II channel were also visible as clear foci in the S5p-
313 channel. Since condensates are of similar size as the resolution limit of conventional optical microscopy,
314 structural details of condensates organization are only apparent with super-resolution methods [19]. We used
315 active focus stabilization and gold fiducials to compensate for sample drift and chromatic aberrations, and
316 aligned general Pol II and S5p 3D dSTORM super-resolution data ~10nm precision (**Methods**). Globally,
317 we find a clustered organization of both, general Pol II and the S5p isoform throughout mESC nuclei
318 (**Fig. 4e,f**) as previously described [2,43]. Condensates are again clearly visible in both channels as large and
319 dense clusters of localizations. We computationally segmented condensate outlines in both channels using
320 the DBSCAN [44] clustering algorithm as previously described [45] (**Fig. 4g-i**), and used alpha-hulls to
321 determine condensate surfaces and volumes. To quantify the degree of overlap between general Pol II and
322 S5p signal in condensate segmentations, we divided the intersection of both volumes by their union (**Fig.**
323 **4j, Suppl. Fig. 11**). We find that in transcription condensates, S5p signal overlapped with general Pol II
324 signal to a high degree. The overlap of S5p-to-general Pol II condensate volumes was comparable to a
325 positive control obtained by labelling Pol II simultaneously with a single primary and two secondary
326 antibodies (**Fig. 4k**). We note that despite the high resolution, it is not possible to directly quantify the
327 degree of Pol II phosphorylation inside condensates from dSTORM data. The stochastic blinking of
328 different fluorophores, immuno-staining and labelling efficiencies, and the repetitive nature of the Pol II
329 CTD all prevent a quantitative interpretation of our data in that regard.

330 Canonically, Pol II is unphosphorylated before it is recruited to the pre-initiation complex on promoter
331 DNA. The S5p mark is deposited when Pol II is loaded onto DNA in the transcription initiation process
332 and retained through initial stages of transcription [11]. The fact that S5p signal fills the volume of
333 transcription condensates therefore strongly supports our hypothesis that the bound mobility fraction
334 inside condensates represents Pol II engaged with chromatin and in an initiating or transcribing state. This
335 finding has important implications for our understanding of transcription condensate organization since it

indicates that Pol II partitioning into condensates can be attributed largely to DNA-binding rather than a phase-separation process mediated by its C-terminal domain.

Fig. 4: Pol II inside condensates is Serine 5-phosphorylated



a Conventional fluorescence image of Snap-Pol II labeled with JFX554, **b** immunofluorescence staining with a general Pol II antibody, and **c** with a Ser5p-specific antibody. **d** Accumulated signal from 12 condensates shows enrichment of all three labels in condensates. **e** Super resolution images of Pol II (**e**) and Ser5p-specific signal (**f**). **g** We determined the outlines of individual condensates in both super-resolved channels and quantified overlap between general Pol II and Ser5p signal. Magnified views of super-resolved general Pol II (**h**) and Ser5p (**i**) signal. **j** Schematic of two channel segmentation overlap quantification (intersection / union). **k** Overlap fraction for Ser5p-PolII (red) (n = 68) and Pol II-Pol II (gray) (n = 22). Ser5p signal overlaps with general Pol II to the same degree as the two-color Pol II labeling positive control (Wilcoxon sum rank test). Scale bars: 2µm (**a**), 500nm (**d**), 200nm (**g**).

Initiation inhibition does not increase Pol II mobility inside condensates

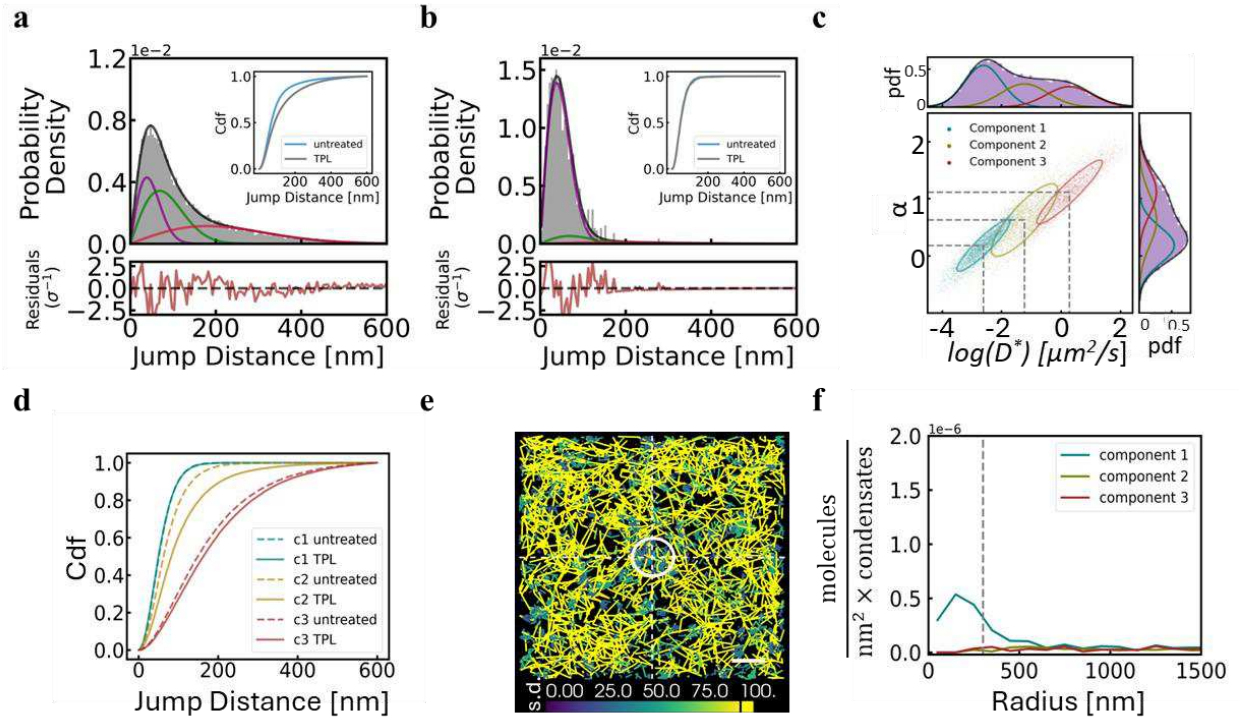
To investigate whether inhibiting transcription initiation would change Pol II mobility inside condensates we treated cells with triptolide. Triptolide blocks interaction of the TFIIH subunit XPB with Pol II in the pre-initiation complex [46]. Prolonged triptolide treatment also leads to Pol II degradation. To avoid artifacts due to Pol II degradation we limited experiments to short incubation times ($10\mu M$ for ≤30 minutes). We then repeated Pol II tracking experiments.

Globally, Pol II mobility was markedly increased under triptolide as compared to untreated cells (**Fig. 5a**). In a jump distance analysis, the high mobility fraction increased to $34.0\% \pm 0.6\%$ (s. d.) ($15.1\% \pm 0.5\%$ in untreated cells) while the fraction of bound particles was reduced to $27.3\% \pm 0.8\%$ ($40.8\% \pm 0.6\%$ in untreated cells). The intermediate low mobility fraction was slightly reduced to $38.7\% \pm 0.9\%$ ($44.1\% \pm 0.9\%$ in untreated cells). These results are expected since inhibiting initiation should reduce the amount of Pol II bound to DNA. A more detailed single trajectory MSD analysis revealed that the three mobility states now separate more clearly in an $\alpha - \log(D^*)$ histogram (**Fig. 5c**). The more mobile populations accounted for larger fractions and shifted towards higher mobility (**Table 1**). This effect is most evident in a plot of the cumulative jump distance distribution functions (CDFs) for each mobility component. The CDFs of the populations C2 (intermediate) and C3 (most mobile) shift to larger displacements, whereas the CDF of the bound component remains virtually unchanged (**Fig. 5d**).

Overall, apparent partitioning of Pol II into condensates was reduced as compared to untreated cells. But the enrichment in condensates remained entirely attributed to the immobile, bound Pol II population as judged by the normalized radial density of tracks (**Fig. 5e,f, Suppl. Fig. 12**). In a jump distance analysis of trajectories fully contained within condensates (**Fig. 5b**), the relative fractions remained unchanged compared to untreated cells (**Suppl. Figs. 6, 13**). A larger fraction of mobile Pol II traversed the condensate volume (**Fig. 5e, Suppl. Fig. 13**), in line with the global increase in the most mobile fraction, but this mobile fraction did not contribute to Pol II enrichment in condensates (**Fig. 5f**). Together, these results show that transcription initiation inhibition raises the mobility of Pol II in the cell nucleus globally,

specifically the mobility and relative abundance of the freely diffusive population. These diffusive molecules can readily access the condensate volume. Pol II concentration remains slightly elevated inside condensates due to DNA binding, possibly representing molecules that were engaged already before drug addition or incomplete suppression of transcription by the drug.

Fig. 5: Initiation inhibition increases Pol II mobility globally.



a Triptolide treatment increases global Pol II mobility as reflected in a jump distance analysis and the comparison of cumulative distribution functions (inset). **b** Inside condensates, the jump distance distribution is unchanged compared to untreated cells. **c** In an α vs log(D^*) plot of single tracks MSD fits, the three mobility states separate more clearly under triptolide treatment. **d** Plotting the CDFs of the three components individually shows that the increased global mobility is due mostly to changes in component 2 (sub-diffusive low mobility, yellow). The freely diffusive component 3 (red) is affected only minimally,

and the bound component 1 (blue) not at all. **e** Color-coding tracks around condensates (white circle) by mobility shows that mobile Pol II (yellow) traverses the condensate volume, but only immobile Pol II (teal) is enriched. **f** This assessment is supported by the normalized radial density distribution of tracks stratified by mobility component. Only the bound component 1 (teal) contributes to Pol II enrichment under triptolide treatment. Scale bar: 500nm (**e**).

Transcription condensates persist in the absence of Pol II

Extended triptolide treatment leads to Pol II degradation [46]. This makes it more difficult to faithfully detect condensates based on Pol II signal. Hence, we labeled a second canonical condensate constituent, the Mediator subunit Med1 [2,15], by heterozygous insertion of a Halo-tag sequence (**Suppl. Fig. 1**). After 100 min incubation, Pol II levels were reduced by ~75% both globally and inside condensates. Mediator signal was affected neither globally nor inside condensates. Condensates remained clearly visible in the Mediator channel even in cells with almost complete Pol II degradation (**Suppl. Fig. 14**). This observation shows that Pol II is dispensable for condensate maintenance. Transcription condensates persist in the absence of Pol II. Together with the fact that the enrichment of Pol II in condensates is due to DNA binding, we conclude that Pol II should be considered a client to an environment created by Mediator condensates and not a structural component of transcription condensate scaffolds.

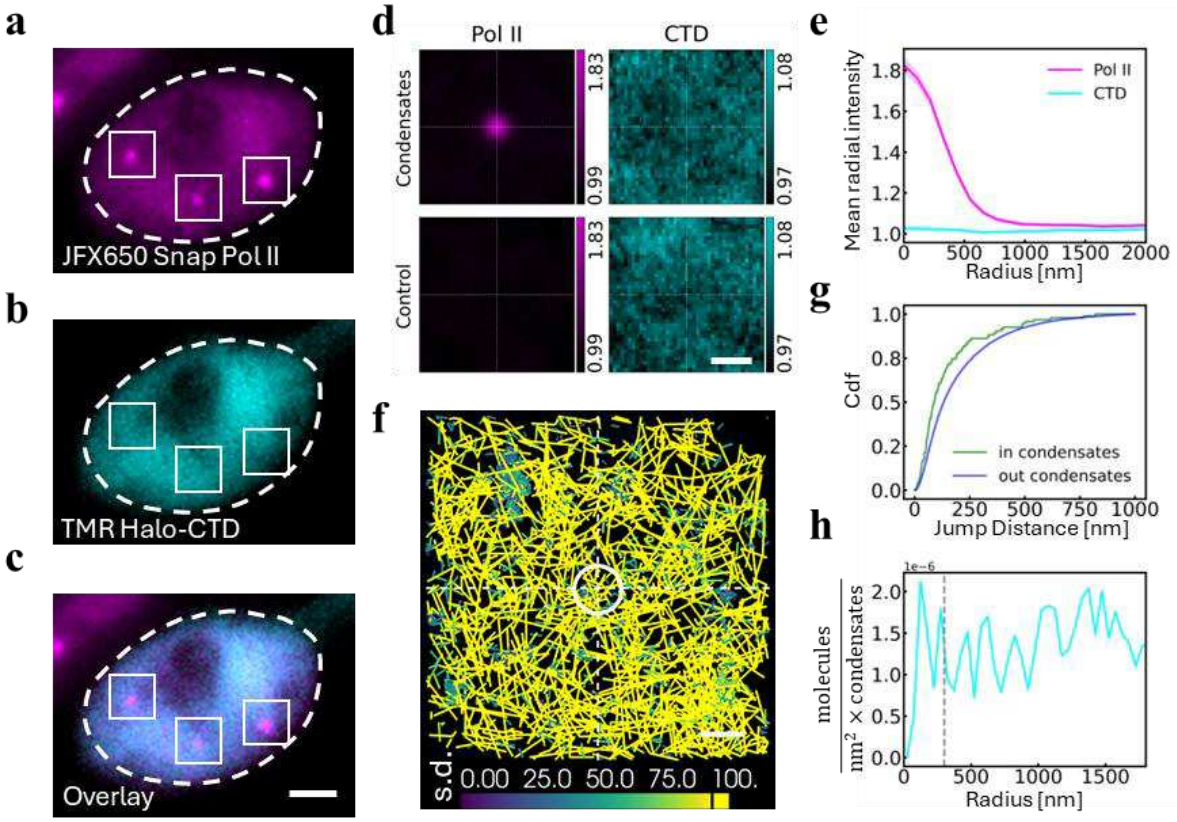
The Pol II CTD contributes only weakly to Pol II partitioning into transcription condensates

The fact that Pol II is dispensable for condensate structural integrity leads us to hypothesize that the Pol II C-terminal domain is not a contributor to multivalent phase separation or condensate maintenance. The prevalent model of transcription condensates [5,29] , proposes that Pol II partitions into endogenous transcription condensates because its CTD forms multivalent interactions with the IDRs of other condensate constituents such as the Brd4 coactivator, transcription factors, and the Mediator complex [4,7,12–15]. If this model is correct, we expect that an exogenous CTD-only construct would enrich inside

endogenous transcription condensates *in vivo*. To test this hypothesis, we transfected SNAP-Pol II cells with a Halo-CTD fusion construct. In transfected cells, the CTD construct appeared homogeneously distributed with a slight enrichment in the cell nucleus over the cytoplasm. We acquired two-color images to determine whether these represent Halo-CTD partitioning into transcription condensates. This was not the case. Even averaging the signal from dozens of condensates showed only minimal enrichment of Halo-CTD signal at endogenous condensates (**Fig. 6 d, f and Suppl. Fig. 16**). The aggregate Halo-CTD fluorescence intensity at condensates was increased <5% over the surrounding nucleoplasm (**Fig. 6f**). *Vice versa*, endogenous Snap-Pol II showed no measurable enrichment at the CTD clusters observed in some cells (**Suppl. Fig. 17**). Tracking single Halo-CTD copies at condensates supports these observations at the single molecule level. While Halo-CTD mobility was slightly reduced inside condensates (**Fig. 6E**), this did not lead to an increase in concentration as judged by track density inside and outside condensates (**Fig. 6H**).

These results confirm that even though Pol II CTD and Mediator droplets coalesce under *in vitro* conditions, this interaction does not drive Pol II partitioning into transcription condensates *in vivo.* We conclude that Pol II may benefit from weak favorable interactions of its CTD with the condensates environment but is ultimately enriched in condensates because other condensate components facilitate Pol II binding to DNA in the condensate environment.

Fig. 6: The Pol II CTD is only weakly enriched in endogenous transcription condensates.



a Two-color imaging of Snap-JFX650-Pol II and **b** Halo-TMR-CTD. **c** Overlay of both channels. **d** Accumulation of condensate signal for Snap-Pol II (top left) and Halo-CTD (top right) at condensate coordinates compared to randomized nuclear coordinates for control (bottom panels). **e**The radial intensity distribution of panels in (D) shows that Halo-CTD is only minimally enriched in endogenous condensates (# of condensates 210). **f** Halo-CTD tracks aligned by condensate center and color-coded by mobility (# of condensates 88, # of tracks 84722). **g** CDF plots of Halo-CTD jump distances inside (green) and outside Pol II condensates (blue) show a small reduction of CTD mobility inside condensates. **h** The radial distribution of single CTD track density around condensates shows no significant enrichment at condensates. Scale bars: 2 µm (**a-c**), 500nm (**d, f**).

Discussion

Biomolecular condensates have been implicated in a plethora of biological processes [47,48]. Condensate formation as a mechanism for self-organization of biomolecules is of particular appeal in the cell nucleus due to the absence of membrane-bound vesicles [49]. Condensate properties have been reported for known nuclear bodies including nucleoli [50], speckles [14], paraspeckles [51], and Cajal bodies [52] as well as condensates associated with specific chromatin transactions [53] like DNA replication [54] and damage repair [55–57], transcription [1,2,58], and RNA processing [59]. Transcription condensates are hotspots of transcription [2] and modulate gene output [3,60–62]. Hence, targeting condensates has emerged as a potential avenue for therapeutic approaches [63–65]. But rational design of therapeutics requires understanding of molecular mechanisms underlying condensate organization in the cell. Studying transcription condensates in their cellular context is particularly challenging because of their small size at or below the diffraction limit of optical microscopy [21]. Reconstituted assays to mimic condensate behavior *in vitro* are naturally limited to a small set of components and cannot recapitulate the full complexity of biomolecular interactions found in the cell. Here, we used single molecule tracking to study how individual constituent molecules interact with endogenous condensates in the nucleus of live cells. We showed that global Pol II mobility is best described by a three-state model ranging from bound to freely diffusing, but Pol II inside condensates is predominantly in a chromatin-bound, Serine 5-phosphorylated state. Mobile Pol II can readily cross condensate boundaries but partitioning into condensates delineated by Mediator foci results from chromatin binding. *In vitro*, the Pol II CTD alone partitions into Mediator droplets through weak and multivalent interactions. But in the cell nucleus, this interaction results in only minor CTD enrichment inside endogenous condensates. The condensate environment persists in the absence of Pol II, suggesting that Pol II is a passive client that does not contribute to the structural maintenance of condensates. Rather, we propose that unbound Pol II entering condensates is rapidly captured and efficiently loaded onto DNA to initiate transcription. The abundance of Mediator inside condensates may facilitate this process since Mediator depletion diminishes Pol II binding in yeast [37]. Notably, the highly efficient loading of Pol II onto DNA in condensates is reminiscent of prior results showing that short-lived transient Pol II clusters

469 at the beta actin gene facilitates this process at maximum efficiency [43]. Our results further imply that
470 endogenous condensates do not exclude chromatin from their interior [10] but harbor transcribed elements
471 in their interior [66]. Biophysically, some biomolecular condensates have been described as porous
472 structures [67]. It is possible that transcription condensates feature interchromatin channels decorated by
473 Brd4 and Mediator that allow mobile Pol II entry favored by weak and multivalent interactions with its C-
474 terminal domain as indicated by *in vitro* experiments. But the high level of Pol II enrichment inside
475 condensates ultimately arises from chromatin binding.

476 Accumulation of RNA Pol II in condensate foci has been reported under various conditions, including
477 heat shock in yeast [68], optically induced synthetic condensates that drive gene expression [60], or
478 transcription factor condensates [7,69–71]. Observing dynamics and functional states of Pol II and other
479 condensate constituents would reveal whether these diverse phenotypes – all described as transcription
480 condensates – indeed represent manifestations of the same molecular mechanism. We anticipate that
481 single molecule approaches will further our mechanistic understanding of condensate function beyond
482 transcription regulation.

483

484

Methods

Cell Culture

Mouse embryonic stem cells (v6.5) were cultured under 2i conditions (ESGRO 2i medium kit, SF016-200, Sigma-Aldrich) with 15 % FBS (Embryomax Fetal bovine serum ES cell Qualified) in 24 well chambers (precoated with 0.1% gelatin for 30 min) at 37°C with 5% CO2.

Cell line generation

We used CRISPR/Cas9 to tag the endogenous Pol II subunit Rpb1 with Snap-Tag and the Mediator subunit Med1 with Halo-Tag. The guide RNAs that target the N-terminus of Rpb1 and Med1 were inserted into a px459v2.0 vector (Addgene #62988) expressing Cas9, the sgRNA, and a Puromycin selection marker (see Suppl. Table 1 for all primer sequences). Repair templates were co-transfected as plasmids constructed through insertion of 500bp homology arms amplified from genomic DNA into the pENTR4-SNAPf vector (Addgene #29652) or pENTR4-HaloTag (Addgene #29644), respectively. We created two versions of the Snap-Rpb1 repair template including a puromycin or hygromycin selection marker flanked by FRT sites for subsequent removal, respectively, followed by a T2A sequence. The Halo-Med1 repair template did not include antibiotic selection markers, but a (GS)2 linker to avoid sterical interference of the HaloTag with Med1. Cells were transfected with 2.5 µg of Px459 V2.0 and 2.5 µg of Hygro-T2A-Snap-Rpb1 repair template plasmid DNA using Xfect™ mESC (Takara Bio, 631320) and treated with puromycin (Sigma, P8833) at 2 µg/ml for two days starting 24h after transfection to select for transfected cells. Surviving cells were treated with hygromycin (Sigma, H3274) at 300 µg/ml for five days. Since we did not find homozygous edits, heterozygous Hygro-T2A-Snap-Rpb1 cells were subsequently transfected with a Puro-T2A-Snap-Rpb1 repair template and exposed to puromycin at a concentration of 2 µg/ml for 5 days. To isolate clonal cell lines, cells were serially diluted into a 96-well plate to single cell concentration and grown for 5 days. 10 well with single colonies were selected for genotyping and a clone with scarless Snap-insertion in both Rpb1 alleles was used for subsequent work.

To insert Halo Tag-Med1 in this background, we followed the same transfection protocol but used fluorescence-assisted cell sorting using Halo-TMR ligand to seed single cell in a 96 well plate. 6 colonies were picked for genotyping. We identified a clone with scarless Halo-Med1 insertion in one allele in the Snap-Pol II background. We note that heterozygous edits reflect low editing frequency (~0.1%). Homozygous edits of both, Rpb1 and Med1, have been demonstrated before and do not impede cell health [15].

Transient expression

We used Gibson assembly (NEB, E5510S) to insert the HaloTag sequence from the pENTR4-HaloTag vector in place of the EGFP sequence in an H2B-GFP vector (Addgene #11680). To construct the Halo-CTD plasmid, we PCR-amplified a sequence comprising the YSPTSPS heptad repeat sequence from the genome of mouse embryonic stem cells and used Gibson assembly to replace the H2B open reading frame in our H2B-Halo plasmid. A flexible $(GS)_2$ linker was inserted between HaloTag and the CTD. We picked clonal colonies for each plasmid and verified full sequences using whole plasmid sequencing (Plasmidsaurus).

Cells were transfected with 500ng plasmid DNA using Lipofectamine (Lipofectamine™ 3000 Transfection Reagent, Thermofisher Scientific) in 24 well plates at 70% confluecny. After 4 hour incubation, transfected cells were transferred to a 35 mm glass-bottom dishes with a 14 mm micro-well (Celvis D35-14-1.5-N). Cells were allowed to recover for 18-24h before imaging.

Cell labelling for imaging experiments

For imaging experiments, cells were plated on 35 mm glass-bottom dishes with a 14 mm micro-well (Celvis D35-14-1.5-N). The imaging dish was coated with PLO (Sigma P4957, diluted 1:1 in water) overnight, followed by coating with Laminin (Sigma L2020 at 0.5µg/ml) for 3 hours prior to cell plating. Cells were allowed to recover overnight (~18h) before imaging. For single particle tracking experiments, cells were incubated with Snap-PAJF646 (120nM, 20 min) followed by Snap-JFX554 (50nM, 20 min) or

Halo-TMR (200nM, 20 min) for Halo-Med1 reference images. Conventional ligands served to obtain reference images for single particle tracking. For widefield imaging after triptolide treatment, cells were incubated with JF646 (500nM) and Halo TMR (200nM) for 20 min. After dye incubation, cells were rinsed briefly with warm cell culture media and incubated for 1 hour in media. Prior to imaging, cells were washed 1X with warm L-15 medium + 15% FBS and imaged in L-15 medium + 15% FBS for a maximum of 1-2 hours. All live cell imaging was done in a stage top incubator (Oko Lab) with humidity control maintained at 37℃. JF dyes were a kind gift from Dr. Luke Lavis, Janelia Research Campus. All fluorophores are listed in Suppl. Table 3.

Triptolide treatment

Triptolide (TPL) pre-diluted in warm imaging medium was added to imaging dishes on the microscope (10μM final concentration). For single particle tracking experiments, the sample was imaged for a maximum of 30 min after TPL addition. To quantify Pol II degradation over longer times, cells were imaged every 10 minutes from the time of triptolide addition up to 110 min with 641nm laser excitation for Snap-Pol II (JF646) and 561nm for Halo-Med1 (TMR).

Single particle tracking

We used the Bruker Vutara 352 platform to perform single particle tracking. The microscope was equipped with a 60X silicon immersion objective. A Hamamatsu ORCA fusion BT camera with 100nm image pixel size was used to collect data in biplane mode with internal compensation for aberrations. Data was recorded at 10ms exposure time in cycles of 1 activation frame (405nm laser at 0.072kW/cm2), 498 frames for tracking (640nm laser at 2.8kW/cm2), and 1 reference frame (561nm laser at 0.075kW/cm2). The reference frame served to identify nuclear outlines and condensate positions. 10-15 cycles were acquired for each field of view until signal from the reference channel was bleached.

We used the ThunderSTORM plugin [32] for ImageJ [72] to localize single molecules in raw .tiff images exported from the Vutara SRX software. A wavelet filter (B-spline) was used for background subtraction

and particles localized with a weighted least squares fit (integrated Gaussian PSF model). Localizations were filtered based on sigma (>100nm), intensity [photons] (>85), and uncertainty (<50nm). Only localizations satisfying all three conditions were considered for subsequent tracking analysis. Condensates were localized in reference frames with filters for sigma >150nm and intensity [photons] > 100.

Further processing and analysis were completed using custom Python scripts. Single molecule localizations were connected to trajectories using a Hungarian algorithm suitable for our sparse localization data (<1.5 localizations/nucleus/frame) with a maximum allowed jump distance of 600nm. Briefly, we compute the pairwise distances between all localizations in consecutive frames. Optimal connections were determined by minimizing the total cost (linear sum of all displacements). We did not allow gap frames. To minimize bias and artifacts, we limited the analysis to 2D coordinates. Jump lengths (displacements) were calculated as Cartesian distances between consecutive localizations in a track.

Jump distance analysis

Jump distance histograms (bin width 5nm) were analyzed by fitting a multi-component probability distribution [73] with custom Python code:

$$P'(r,t)dr = \sum_{k=1}^{n} \frac{f_k}{2(D_k t + \sigma^2)} e^{\frac{-r^2}{4(D_k t+\sigma^2)}} r dr$$

where f_k is the relative fraction, D_k the diffusion coefficient, and σ the single molecule localization error. We determined $\sigma = 22nm$ from fixed cell experiments acquired under otherwise identical conditions. To determine the number of mobility states, we calculated Bayesian Information Criterion (BIC) scores for $n = 1-5$. A three-state model yielded the lowest BIC score.

To compare jump distance histograms for untreated and triptolide conditions, we first performed a global fit by pooling an equal number of jumps (25,000) randomly chosen from each condition. We used this pooled dataset to determine diffusion coefficients in the three-state model. The procedure was repeated 50 times, and we report the mean and standard deviation for each fit parameter. We then fixed the values for

D_k and used only f_k as free fit parameters while fitting the jump distance histograms for each condition individually and compare relative fractions in our discussion of results.

Single trajectory mean square displacement analysis

Mean square displacement analysis of single trajectories was performed using custom-written Python code. Only tracks of length five jumps or longer were analyzed. We calculated the mean square displacement (MSD) as a function of lag time for each track and fitted the first four data points (up to $\Delta t = 40ms$) with the power law equation $MSD(\Delta t) = 4D^*\Delta t^{\alpha}$ to obtain values for the effective diffusion coefficient D^* and the anomalous exponent α for each track. We generated a 2D histogram of $\log(D^*)$ vs α and fitted the data distribution with a Gaussian mixture model (GMM) using the scikit-learn library [74]. BIC scores again indicated a three-state model as the best fit for Pol II tracking data. H2B tracking data was best fit by a two-state model. We assigned each track to one of the states based on the amplitude of the three Gaussians at its parameters.

Track classification

To relate tracks to condensates, we subtracted condensate center coordinates for the respective cycle from Pol II track coordinates observed in the same cycle. This allowed us to readily calculate the radial distance of each coordinate from the condensate center. Tracks fully contained within a 300nm radius from the condensate center were considered as inside condensates. Tracks with no coordinate inside a 300nm radius were considered as outside tracks. Tracks containing localizations both inside and outside the boundary are considered crossing trajectories. Separately, we classified individual displacements rather than full tracks using the same criteria.

Radial Density Analysis

Radial molecule density around condensates was calculated by dividing the number of tracks in a radial annulus by the area of the annulus (radial bin width 100nm). To avoid overcounting bound molecules that

yield more localizations, we considered only the mean coordinate of each track. The density of tracks was further normalized by the number of condensates observed to compare conditions. Fold enrichment inside condensates is calculated by dividing the density the tracks within 250nm by the density of the tracks in a region 700-1800 nm from the center of the condensates.

Nuclear segmentation in widefield images

Nuclear segmentation was performed with Stardist2D using the pre-trained model, '2D_versatile_fluo' with input parameters, scale = 0.3, prob_thresh = 0 .40, nms_thresh = 0.01. Nuclear labels smaller than 3000 pixels (~36 μm2 area) were discarded. Nuclear segmentations were used to exclude any spurious cytoplasmic signal in tracking analysis.

Condensate detection in widefield images

Custom-written python code was used to detect condensates in widefield images. Intensity peaks were identified using scipy's [75] Laplacian of Gaussian filter and binarized using intensity thresholding. Regions with an area of less than 20 pixels were discarded. For remaining candidate regions, we determined the convex hull outline using *scikit-image*'s convex_hull function, and measured the eccentricity, centroid, mean intensity, and local background intensity (median value of pixel intensities at a distance of 2 pixels outside the segmented foci). Condensates were identified as regions with eccentricity < 0.86 and a ratio of peak mean intensity to background intensity > 1.15. This procedure ensured that the brightest, unambiguous condensate foci were reliably identified. Signal from multiple condensates was aligned based on centroid coordinates with pixel precision for aggregate analysis.

Immunostaining for dSTORM imaging

Cells were plated in 8-well slides with coverglass bottom (Celvis #C8-1.5H-N) coated with PLO/lamining as described above. Cells were fixed with 100% ice-cold methanol for 7 min at -20℃ and washed 3X with cold PBS (4 ℃) for 2 min each. Cells were then permeabilized with 0.1 % Triton-X 100 in PBS for 10

min followed by 3 washes with PBS (5 min each) and blocking for 1h at room temperature (4% BSA in PBS). Primary antibody was incubated at 4℃ overnight (~18h) in a humidified chamber. The next day, cells were washed 3X with PBS (5 min each), and incubated with secondary antibody for 1 hour at room temperature. Samples were then washed 3X with PBS. See Suppl. Table 2 for antibodies and concentrations.

Super-resolution Microscopy

Gold fiducials were added for drift correction and chromatic channel alignment during super-resolution imaging. 15 µl of 100nm gold fiducial solution (TED PELLA cat#. 15711-20) was diluted in 105 µl of PBS. The solution was vortexed for ~5 seconds, sonicated for 10 minutes, and vortexed again for ~ 5 seconds. The solution was added directly to the imaging dish, aspirated after 10 minutes, and washed 2x with PBS. Two-color dSTORM buffer was prepared as described in [76] on ice. Briefly, 30 µl of OxyFlour (Oxyrase Inc., Mansfield, Ohio, U.S.A) was mixed with 680 µl of PBS kept at 4C. 50 µl of sodium DL-lactate (Sigma #L1375) was added and vortexed. 50 µl of 1M MEA (Sigma #30070) was added (final concentration 50 mM MEA). Finally, 40 µl of NaOH was added to maintain the pH at ~8.0. The buffer was filtered using a 0.2 µm syringe filter. At least 200 µl of imaging buffer was added to the dish for imaging. Imaging buffer was used only on the day of preparation.

Data acquisition and single-molecule localization were performed using Bruker's SRX software with vfocus focus stabilization activated. The sequential acquisition method was employed to record images with 640nm laser activation (5.3 kW/cm^2) for AF647 and 488nm (5kW/cm^2) for AF488 fluorophores. For each color channel, 50,000 frames were acquired at 20ms exposure time in biplane mode. Localizations with low confidence were ignored using advanced filters available in SRX (axial precision <100nm, relative z range ± 500nm, psf radial offset <100nm, photon count). Drift and chromatic aberrations were corrected using gold fiducial localizations within the SRX software. Individual nuclei were manually segmented, and localizations were exported in .mat format for further analysis in Python.

Condensate identification and overlap fraction measurement in super resolution

Scikit-learn's DBSCAN function was used to segment clusters in the super-resolution localization data. We used corresponding widefield reference images to determine optimal DBSCAN parameters ($\epsilon = 70 - 150\ nm,$ min_points $= 6 - 12$), for condensate identification. This procedure was completed in each super-resolution channel independently. We computed the intersection and union of the alpha hull of segmented condensate volumes in each channel using *pyvista*'s Boolean operation functions. To compute the overlap fraction, we divided the intersection by the union of individual condensate volumes in both channels.

Statistical information

To determine error bars for jump distance distribution fits, we randomly sampled 25,000 jumps from the respective full distribution and repeated the fitting procedure 50 times. From these 50 iterations, we computed mean and standard error of the mean. For comparison of other parameter distributions, we used the two-sided Wilcoxon rank-sum test.

Data Availability

Sample tracking data sets that this code was used on are available through the Spille Lab FigShare [link will be inserted]. Plasmids (Halo-CTD, H2B-Halo) will be deposited through Addgene. Requests for cell lines and other resources should be addressed to the corresponding author.

Code Availability

Custom analysis code written in Python with usage instructions is available through the Spille Lab GitHub site [link will be inserted].

References

1. Sabari, B. R. *et al.* Coactivator condensation at super-enhancers links phase separation and gene control. *Science* eaar3958 (2018) doi:10.1126/science.aar3958.
2. Cho, W.-K. *et al.* Mediator and RNA polymerase II clusters associate in transcription-dependent condensates. *Science* eaar4199 (2018) doi:10.1126/science.aar4199.
3. Du, M. *et al.* Direct observation of a condensate effect on super-enhancer controlled gene bursting. *Cell* **187**, 331-344.e17 (2024).
4. Boija, A. *et al.* Transcription Factors Activate Genes through the Phase-Separation Capacity of Their Activation Domains. *Cell* **175**, 1842-1855.e16 (2018).
5. Ryu, K., Park, G. & Cho, W.-K. Emerging insights into transcriptional condensates. *Exp Mol Med* **56**, 820–826 (2024).
6. Basu, S. *et al.* Unblending of Transcriptional Condensates in Human Repeat Expansion Disease. *Cell* **181**, 1062-1079.e30 (2020).
7. Lyons, H. *et al.* RNA polymerase II partitioning is a shared feature of diverse oncofusion condensates. *Cell* **0**, (2025).
8. Henninger, J. E. *et al.* RNA-Mediated Feedback Control of Transcriptional Condensates. *Cell* **184**, 207-225.e24 (2021).
9. Chong, S. *et al.* Imaging dynamic and selective low-complexity domain interactions that control gene transcription. *Science* **361**, eaar2555 (2018).
10. Shin, Y. *et al.* Liquid Nuclear Condensates Mechanically Sense and Restructure the Genome. *Cell* **175**, 1481-1491.e13 (2018).
11. Hsin, J.-P. & Manley, J. L. The RNA polymerase II CTD coordinates transcription and RNA processing. *Genes & Development* **26**, 2119 (2012).

12. Boehning, M. *et al.* RNA polymerase II clustering through carboxy-terminal domain phase separation. *Nat Struct Mol Biol* **25**, 833–840 (2018).
13. Kwon, I. *et al.* Phosphorylation-Regulated Binding of RNA Polymerase II to Fibrous Polymers of Low-Complexity Domains. *Cell* **155**, 1049–1060 (2013).
14. Guo, Y. E. *et al.* Pol II phosphorylation regulates a switch between transcriptional and splicing condensates. *Nature* **572**, 543–548 (2019).
15. Sabari, B. R. *et al.* Coactivator condensation at super-enhancers links phase separation and gene control. *Science* **361**, eaar3958 (2018).
16. C, L. *et al.* Light-induced targeting enables proteomics on endogenous condensates. *Cell* **187**, (2024).
17. Lyons, H. *et al.* Functional partitioning of transcriptional regulators by patterned charge blocks. *Cell* **186**, 327-345.e28 (2023).
18. Stortz, M., Presman, D. M. & Levi, V. Transcriptional condensates: a blessing or a curse for gene regulation? *Commun Biol* **7**, 1–10 (2024).
19. McSwiggen, D. T., Mir, M., Darzacq, X. & Tjian, R. Evaluating phase separation in live cells: diagnosis, caveats, and functional consequences. *Genes Dev.* (2019) doi:10.1101/gad.331520.119.
20. Amitai, A. Chromatin Configuration Affects the Dynamics and Distribution of a Transiently Interacting Protein. *Biophysical Journal* **114**, 766–771 (2018).
21. Pandey, G., Budhathoki, A. & Spille, J.-H. Characterizing Properties of Biomolecular Condensates Below the Diffraction Limit In Vivo. in *Phase-separated Biomolecular Condensates* (Springer, 2022).
22. Ladouceur, A.-M. *et al.* Clusters of bacterial RNA polymerase are biomolecular condensates that assemble through liquid–liquid phase separation. *PNAS* **117**, 18540–18549 (2020).
23. McSwiggen, D. T. *et al.* Evidence for DNA-mediated nuclear compartmentalization distinct from phase separation. *eLife* **8**, e47098 (2019).

24. Kent, S. *et al.* Phase-Separated Transcriptional Condensates Accelerate Target-Search Process Revealed by Live-Cell Single-Molecule Imaging. *Cell Reports* **33**, 108248 (2020).
25. Hao, S. *et al.* YAP condensates are highly organized hubs. *iScience* **27**, 109927 (2024).
26. Keppler, A., Pick, H., Arrivoli, C., Vogel, H. & Johnsson, K. Labeling of fusion proteins with synthetic fluorophores in live cells. *Proceedings of the National Academy of Sciences* **101**, 9955–9959 (2004).
27. Grimm, J. B. *et al.* Bright photoactivatable fluorophores for single-molecule imaging. *Nat Methods* **13**, 985–988 (2016).
28. Grimm, J. B. *et al.* A General Method to Improve Fluorophores Using Deuterated Auxochromes. *JACS Au* **1**, 690–696 (2021).
29. Rippe, K. & Papantonis, A. RNA polymerase II transcription compartments — from factories to condensates. *Nat Rev Genet* 1–14 (2025) doi:10.1038/s41576-025-00859-6.
30. Los, G. V. *et al.* HaloTag: A Novel Protein Labeling Technology for Cell Imaging and Protein Analysis. *ACS Chem. Biol.* **3**, 373–382 (2008).
31. Hansen, A. S. *et al.* Robust model-based analysis of single-particle tracking experiments with Spot-On. *eLife Sciences* **7**, e33125 (2018).
32. Ovesný, M., Křížek, P., Borkovec, J., Svindrych, Z. & Hagen, G. M. ThunderSTORM: a comprehensive ImageJ plug-in for PALM and STORM data analysis and super-resolution imaging. *Bioinformatics* **30**, 2389–2390 (2014).
33. Matsuoka, S., Shibata, T. & Ueda, M. Statistical analysis of lateral diffusion and multistate kinetics in single-molecule imaging. *Biophys J* **97**, 1115–1124 (2009).
34. Schwarz, G. Estimating the Dimension of a Model. *The Annals of Statistics* **6**, 461–464 (1978).
35. Hansen, A. S. *et al.* Robust model-based analysis of single-particle tracking experiments with Spot-On. *Elife* **7**, e33125 (2018).

36. Abrahamsson, S. *et al.* Fast multicolor 3D imaging using aberration-corrected multifocus microscopy. *Nat Methods* **10**, 60–63 (2013).
37. Nguyen, V. Q. *et al.* Spatiotemporal coordination of transcription preinitiation complex assembly in live cells. *Molecular Cell* **81**, 3560-3575.e6 (2021).
38. Mazzocca, M. *et al.* Chromatin organization drives the search mechanism of nuclear factors. *Nat Commun* **14**, 6433 (2023).
39. Nagashima, R. *et al.* Single nucleosome imaging reveals loose genome chromatin networks via active RNA polymerase II. *J Cell Biol* **218**, 1511–1530 (2019).
40. Wagh, K. *et al.* Dynamic switching of transcriptional regulators between two distinct low-mobility chromatin states. *Science Advances* **9**, eade1122 (2023).
41. Chu, F.-Y., Clavijo, A. S., Lee, S. & Zidovska, A. Transcription-dependent mobility of single genes and genome-wide motions in live human cells. *Nat Commun* **15**, 8879 (2024).
42. van de Linde, S. *et al.* Direct stochastic optical reconstruction microscopy with standard fluorescent probes. *Nat Protoc* **6**, 991–1009 (2011).
43. Cho, W.-K. *et al.* RNA Polymerase II cluster dynamics predict mRNA output in living cells. *Elife* **5**, e13617 (2016).
44. Ester, M., Kriegel, H.-P., Sander, J. & Xu, X. A density-based algorithm for discovering clusters in large spatial databases with noise. in *Proceedings of the Second International Conference on Knowledge Discovery and Data Mining* 226–231 (AAAI Press, Portland, Oregon, 1996).
45. Andrews, J. O. *et al.* qSR: a quantitative super-resolution analysis tool reveals the cell-cycle dependent organization of RNA Polymerase I in live human cells. *Scientific Reports* **8**, 7424 (2018).
46. Titov, D. V. *et al.* XPB, a Subunit of TFIIH, Is a Target of the Natural Product Triptolide. *Nat Chem Biol* **7**, 182–188 (2011).

47. Banani, S. F., Lee, H. O., Hyman, A. A. & Rosen, M. K. Biomolecular condensates: organizers of cellular biochemistry. *Nature Reviews Molecular Cell Biology* **18**, 285–298 (2017).
48. Hyman, A. A., Weber, C. A. & Jülicher, F. Liquid-Liquid Phase Separation in Biology. *Annual Review of Cell and Developmental Biology* **30**, 39–58 (2014).
49. Sabari, B. R., Dall'Agnese, A. & Young, R. A. Biomolecular Condensates in the Nucleus. *Trends in Biochemical Sciences* **45**, 961–977 (2020).
50. Brangwynne, C. P., Mitchison, T. J. & Hyman, A. A. Active liquid-like behavior of nucleoli determines their size and shape in Xenopus laevis oocytes. *PNAS* **108**, 4334–4339 (2011).
51. Fox, A. H., Nakagawa, S., Hirose, T. & Bond, C. S. Paraspeckles: Where Long Noncoding RNA Meets Phase Separation. *Trends in Biochemical Sciences* **43**, 124–135 (2018).
52. Sawyer, I. A., Hager, G. L. & Dundr, M. Specific genomic cues regulate Cajal body assembly. *RNA Biology* **14**, 791–803 (2017).
53. Agbleke, A. A. *et al.* Advances in Chromatin and Chromosome Research: Perspectives from Multiple Fields. *Molecular Cell* **79**, 881–901 (2020).
54. Parker, M. W. *et al.* A new class of disordered elements controls DNA replication through initiator self-assembly. *eLife* **8**, e48562 (2019).
55. Dall'Agnese, G. *et al.* Role of condensates in modulating DNA repair pathways and its implication for chemoresistance. *Journal of Biological Chemistry* **299**, (2023).
56. Kilic, S. *et al.* Phase separation of 53BP1 determines liquid-like behavior of DNA repair compartments. *The EMBO Journal* **38**, e101379 (2019).
57. Wang, Y.-L. *et al.* Liquid-liquid phase separation in DNA double-strand breaks repair. *Cell Death Dis* **14**, 1–10 (2023).
58. Hnisz, D., Shrinivas, K., Young, R. A., Chakraborty, A. K. & Sharp, P. A. A Phase Separation Model for Transcriptional Control. *Cell* **169**, 13–23 (2017).

59. Galganski, L., Urbanek, M. O. & Krzyzosiak, W. J. Nuclear speckles: molecular organization, biological function and role in disease. *Nucleic Acids Res* **45**, 10350–10368 (2017).
60. Wei, M.-T. *et al.* Nucleated transcriptional condensates amplify gene expression. *Nat Cell Biol* **22**, 1187–1196 (2020).
61. Pei, G., Lyons, H., Li, P. & Sabari, B. R. Transcription regulation by biomolecular condensates. *Nat Rev Mol Cell Biol* **26**, 213–236 (2025).
62. Henninger, J. E. *et al.* RNA-Mediated Feedback Control of Transcriptional Condensates. *Cell* **184**, 207-225.e24 (2021).
63. Klein, I. A. *et al.* Partitioning of cancer therapeutics in nuclear condensates. *Science* **368**, 1386–1392 (2020).
64. Han, T. W., Portz, B., Young, R. A., Boija, A. & Klein, I. A. RNA and condensates: Disease implications and therapeutic opportunities. *Cell Chemical Biology* **31**, 1593–1609 (2024).
65. Mitrea, D. M., Mittasch, M., Gomes, B. F., Klein, I. A. & Murcko, M. A. Modulating biomolecular condensates: a novel approach to drug discovery. *Nat Rev Drug Discov* **21**, 841–862 (2022).
66. Pancholi, A. *et al.* RNA polymerase II clusters form in line with surface condensation on regulatory chromatin. *Molecular Systems Biology* **17**, e10272 (2021).
67. Rippe, K. Liquid-Liquid Phase Separation in Chromatin. *Cold Spring Harb Perspect Biol* **14**, a040683 (2022).
68. Chowdhary, S., Paracha, S., Dyer, L. & Pincus, D. Emergent 3D genome reorganization from the stepwise assembly of transcriptional condensates. 2025.02.23.639564 Preprint at https://doi.org/10.1101/2025.02.23.639564 (2025).
69. Nair, S. J. *et al.* Phase separation of ligand-activated enhancers licenses cooperative chromosomal enhancer assembly. *Nature Structural & Molecular Biology* **26**, 193 (2019).

70. Zhang, F. *et al.* Dynamic phase separation of the androgen receptor and its coactivators key to regulate gene expression. *Nucleic Acids Res* **51**, 99–116 (2022).
71. Cai, D. *et al.* Phase separation of YAP reorganizes genome topology for long-term YAP target gene expression. *Nat Cell Biol* **21**, 1578–1589 (2019).
72. Schneider, C. A., Rasband, W. S. & Eliceiri, K. W. NIH Image to ImageJ: 25 years of image analysis. *Nat Methods* **9**, 671–675 (2012).
73. Siebrasse, J. P. *et al.* Discontinuous movement of mRNP particles in nucleoplasmic regions devoid of chromatin. *Proceedings of the National Academy of Sciences* **105**, 20291–20296 (2008).
74. Pedregosa, F. *et al.* Scikit-learn: Machine Learning in Python. *J. Mach. Learn. Res.* **12**, 2825–2830 (2011).
75. Virtanen, P. *et al.* SciPy 1.0: fundamental algorithms for scientific computing in Python. *Nat Methods* **17**, 261–272 (2020).
76. Nahidiazar, L., Agronskaia, A. V., Broertjes, J., Broek, B. van den & Jalink, K. Optimizing Imaging Conditions for Demanding Multi-Color Super Resolution Localization Microscopy. *PLOS ONE* **11**, e0158884 (2016).

Acknowledgements

We thank Wei Fang and the University of Illinois Chicago Flow Cytometry Core for assistance with FACS sorting. We thank Luke D. Lavis, Jonathan B. Grimm, and the Open Chemistry team (Janelia Research Campus) for the Janelia Fluor dyes. We gratefully acknowledge support through a UIC Honors College Research Grant (G.H.N.), the UIC LASURI scholarship program (S.M., G.H.N.), and the UIC Chancellor's Undergraduate Research Award program (S.M.). J.H.S. acknowledges support from the Research Corporation for Scientific Advancement (CMC 28407), the NIH (R35GM150560), and the University of Illinois Chicago Startup Fund.

Ethics declarations

The authors declare no conflicts of interest.

Supplementary Information

Supplementary Information:

Supplementary Figures 1-20

Supplementary Tables 1-3

Supplementary Videos 1-3

Tables

Table 1: Global Pol II mobility states from single-track MSD analysis

Parameter	Control	TPL
f_1 (bound)	57.5%	43.4%
α_1	0.177 ± 0.003	0.184 ± 0.004
$\langle \log (D_1^*) \rangle$	-2.613 ± 0.005	-2.615 ± 0.008
$\langle D_1^* \rangle$ $[\mu m^2/s^\alpha]$	0.0024	0.0024
f_2 (subdiffusive)	23.6%	30.3%
α_2	0.592 ± 0.005	0.628 ± 0.007
$\langle \log (D_2^*) \rangle$	-1.643 ± 0.009	-1.236 ± 0.013
$\langle D_2^* \rangle$ $[\mu m^2/s^\alpha]$	0.023	0.058
f_3 (diffusive)	18.9%	26.3%
α_3	0.945 ± 0.006	1.118 ± 0.007
$\langle \log(D_3^*) \rangle$	-0.108 ± 0.012	0.278 ± 0.013
$\langle D_3^* \rangle$ $[\mu m^2/s^\alpha]$	0.78	1.89

Errors in the tables represent s.e.m calculated.

Pol II Untreated: 13 independent samples, # of dishes = 16, # of nuclei = 269, # of tracks with length >5 = 28267, # of tracks in component 1 = 15310, # of tracks in component 2 = 7499, # of tracks in component 3 = 5458.

Pol II TPL: 8 independent samples, # of dishes = 22, # of nuclei = 361, # of tracks with length >5 = 12229, # of tracks in component 1 = 5339, # of tracks in component 2= 3547, # of tracks in component 3 = 3343.

Supplementary Files

This is a list of supplementary files associated with this preprint. Click to download.

- SupplementaryVideo1.singlepolIItracks.mp4
- SupplementaryVideo2.PolIItrackswithcondensatesinglecell.mp4
- SupplementaryVideo3.PolIIaggregatedtrajectories.mp4
- Supplementarymaterialssubmission.pdf